# Data-driven Multi-mode Adaptive Operation of Soft Open Point with Measuring Bad Data

Shiyuan Gao, *Graduate Student Member*, *IEEE*, Peng Li, *Senior Member*, *IEEE*, Haoran Ji*, *Member*, *IEEE*, Jinli Zhao, *Member*, *IEEE*, Hao Yu, *Senior Member, IEEE*, Jianzhong Wu, *Fellow, IEEE*, and Chengshan Wang, *Senior Member*, *IEEE*

***Abstract*—The high penetration of distributed generators (DGs) deteriorates the uncertainty of active distribution networks (ADNs). Soft open points (SOPs) can effectively improve flexibility and deal with operational issues in ADNs. However, the formulation of SOP control strategies depends on the accurate mechanism model. Data-driven method can utilize only measuring data to conduct operation and becomes a promising way. In practical conditions, the measuring data may suffer from bad data and measuring errors, which poses a challenge to meet the diverse operational requirements. This paper proposes a data-driven multi-mode adaptive control method for SOP with measuring bad data. First, considering the inaccurate network parameters and quality of measuring data, a robust data-driven framework for SOP operation is proposed based on robust hierarchical-optimization recursive least squares (HO-RLS). Then, a multi-mode control strategy for SOP is proposed to adapt to the diverse operational requirements. A dynamic triggering mechanism is designed to achieve adaptive mode switching. The case studies on practical distribution networks show that the proposed method can fully explore the benefits of SOP to improve the operational performance of ADNs. The potential limitations are discussed to enhance practicality.**

***Index Terms*—active distribution networks (ADNs), soft open points (SOPs), data-driven, bad data, multi-mode adaptive control.**

## NOMENCLATURE

| | |
|---|---|
| ***Sets*** | |
| $\mathcal{N}$ | Set of all nodes in ADNs |
| $\mathcal{L}$ | Set of all lines in ADNs |
| $\mathcal{G}$ | Set of all DGs in ADNs |
| $\mathcal{S}$ | Set of all SOPs in ADNs |
| $\Omega_{\mathrm{O}}$ | Set of all control modes |
| $\Omega_{\mathrm{m}}$ | Set of all SOP converters |
| ***Indices*** | |
| $i, j$ | Index of nodes |
| $ij$ | Index of lines |
| $t$ | Index of time periods |
| $m$ | Index of measurements |
| $u$ | Index of time window |
| ***Variables*** | |
| $\boldsymbol{y}_t, \widetilde{\boldsymbol{y}}_t$ | Expected and actual measurement vector at period $t$ |
| $\boldsymbol{x}_t$ | Strategy of SOP at period $t$ |
| $\boldsymbol{F}_t, \boldsymbol{F}'_t$ | Expected and actual response functions at period $t$ |
| $\boldsymbol{q}_t$ | Auxiliary optimization vector of SOP at period $t$ |
| $\boldsymbol{o}_t, \widehat{\boldsymbol{o}}_t$ | Real and estimated bad data vectors at period $t$ |
| $\boldsymbol{\varepsilon}_t$ | Measurement error at period $t$ |
| $\widehat{\boldsymbol{F}}'_t$ | Estimated response function at period $t$ |
| $\tau_k$ | Bad data step size of the $k$-th iteration |
| $\boldsymbol{U}_t, \boldsymbol{y}_t^{\mathrm{U}}$ | Actual and measured nodal voltage vector at period $t$ |
| $\boldsymbol{I}_t$ | Actual line current vector at period $t$ |
| $\boldsymbol{y}_t^{\mathrm{L}}$ | Equivalent measurement value of current loading vector at period $t$ |
| $\boldsymbol{y}_t^{\mathrm{P}}$ | Equivalent measurement value of square of line current vector at period $t$ |
| $\omega_t^{\mathrm{U}}, \omega_t^{\mathrm{L}}, \omega_t^{\mathrm{P}}, \omega_t^{\mathrm{M}}$ | Switching flag of Modes I, II, III, and IV at period $t$ |
| $C_{\mathrm{U}}, C_{\mathrm{L}}$ | Voltage deviation cost, current loading deviation cost of state variation between $t$ and $t-1$ |
| $P_{t,i}^{\mathrm{SOP}}, Q_{t,i}^{\mathrm{SOP}}$ | Active and reactive power injection by SOP at node $i$ at period $t$ |
| $P_{t,i}^{\mathrm{SOP,L}}$ | Power loss of SOP at node $i$ at period $t$ |
| $S_i^{\mathrm{SOP}}$ | Capacity limit of SOP at node $i$ |
| ***Parameters*** | |
| $N$ | Number of all nodes |
| $N_{\mathrm{DG}}$ | Number of all DGs |
| $N_{\mathrm{SOP}}$ | Number of all SOPs |
| $M$ | Number of all measurements |
| $\lambda_u$ | Weight coefficient of bad data |
| $t_0$ | Initial time period |
| $\lambda_{\mathrm{LASSO}}$ | LASSO regression coefficient |
| $\tau_{\max}, \tau_{\min}$ | Maximum and minimum values of iteration step size |
| $\boldsymbol{y}^{\mathrm{U,ref}}$ | Nodal voltage reference |
| $\boldsymbol{I}_{\max}$ | Rated line current vector |
| $\boldsymbol{I}^{\mathrm{thr}}$ | Maximum of optimized line current vector |
| $\boldsymbol{y}^{\mathrm{L,ref}}$ | Current loading reference vector |
| $\boldsymbol{y}^{\mathrm{P,ref}}$ | Square of line current reference vector |
| $\boldsymbol{U}_{\max}, \boldsymbol{U}_{\min}$ | Maximum and minimum values of voltage vector |
| $\boldsymbol{U}_{\max}^{\mathrm{thr}}, \boldsymbol{U}_{\min}^{\mathrm{thr}}$ | Maximum and minimum values of optimized voltage vector |

This work was supported by the National Natural Science Foundation of China (U22B20114), Key Project of Tianjin Natural Science Foundation (22JCZDJC00700).(*Corresponding author: Haoran Ji*)

S. Gao, P. Li, H. Ji, J. Zhao, H. Yu and C. Wang are with the Key Laboratory of Smart Grid of Ministry of Education, Tianjin University, Tianjin 300072, China (email: gaosy@tju.edu.cn; lip@tju.edu.cn; jihaoran@tju.edu.cn; jlzhao@tju.edu.cn; tjuyh@tju.edu.cn; cswang@tju.edu.cn).

J. Wu is with the Institute of Energy, School of Engineering, Cardiff University, Cardiff CF24 3AA, U.K. (email: wuj5@cardiff.ac.uk).

| | |
|---|---|
| $Q_{i,\max}^{\mathrm{SOP}}$, $Q_{i,\min}^{\mathrm{SOP}}$ | Maximum and minimum values of reactive power injection of SOP at node $i$ |
| $T$ | Optimization time |
| $\Delta T$, $\Delta t$ | Optimization/control horizon |

## I. Introduction

HIGH penetration of distributed generators (DGs) deteriorates the uncertainty and variability of active distribution networks (ADNs), which causes reverse power flows and severe voltage fluctuations [1]. Power electronic devices, represented by soft open points (SOPs) [2], can accurately regulate the active and reactive power flow of the connected feeders. SOP is expected to become a vital physical foundation of distribution networks to deal with the operational issues caused by DG integration [3]. However, day-ahead operation of SOP may be difficult to deal with the frequent voltage fluctuations in complex operational environments [4]. The rapid and efficient control is still the main concern for SOP operation [5].

Extensive studies have been conducted on the intra-day control of SOP, such as robust operation [6], coordinated control [7], [8], etc. The authors in [9] proposed a two-layer control strategy for SOP to improve the economy and reliability of system. A two-stage optimization framework was proposed in [10] for the optimal installation and operation of SOPs to defend systems against load-altering attacks. The authors in [11] proposed a real-time coordinated method for SOP and electric vehicles with multiple time scales under uncertainties. However, in practical applications, the above model-based methods are dependent on accurate mechanism models and parameters, which may be difficult to obtain in practical ADNs, especially with the increasing complexity and numerous components [12]. Therefore, a more intelligent control method for SOP is crucial in the absence of network parameters.

With the rapid development of digitization level and communication technologies, distribution phasor measurement unit (D-PMU) [13] and supervisory control and data acquisition systems (SCADA) [14] have gradually been deployed in distribution networks. Sufficient real-time measurement data can be acquired, which provides an opportunity to realize optimization without accurate parameters or physical models of ADNs. The heterogeneous measurements contain important operational information such as the system status and operational trend [15]. Developing a data-driven model, fully utilizing the operational data, and optimizing the strategies of flexibility resources in complex scenarios have become essential in improving operational performance.

Data-driven methods that rely only on measurement or historical data to optimize the system operation have attracted widespread attention. Such methods can be divided into two categories: machine learning methods and iterative control methods. Machine learning methods train the neural network models offline using the historical data, which are then applied online with real-time data input [16], [17]. The authors in [18] proposed a multi-agent deep reinforcement learning-based approach to enhance the control capability under various operation conditions. The authors in [19] proposed a decomposition and coordination reinforcement learning algorithm based on a federated learning framework with a satisfactory learning convergence. A multi-mode data-driven voltage control strategy based on a convolution neural network was proposed in [20], which provided a novel control mode. However, the training of machine learning models may be a time-consuming process and lacks the adaptability to environment changing. If the network topology changes, the model needs to be retrained to adapt to the changes. In contrast, operational strategies based on iterative control methods can be formulated online according to real-time measurements to deal with inaccurate model parameters and the DG fluctuations.

Data-driven control methods of ADNs have been preliminarily studied. Considering the inaccuracy of parameters, the authors in [21] proposed a data-driven operational strategy for SOPs based on model-free adaptive control, which improved the operational performance. The authors in [22] proposed a data-driven estimation method of voltage-to-power Sensitivities, which considered mutual dependency of the sensitivities and achieved high accuracy. Ref. [23] employed a hysteresis control strategy for data-driven voltage-VAR sequential control to avoid frequent control actions. The novel data-driven robust hierarchical-optimization recursive least squares (HO-RLS) method proposed in [24] could accurately describe the input-output relationship of the system and eliminate the impact of bad data. Ref. [25] further applied the robust HO-RLS method to control multiple virtual power plants to realize data-driven distributed voltage control, which improved the control robustness.

As for the data-driven control of SOPs, further research is required on the following aspects. a) Data driven methods lack effective guidance information. The quality of measuring data can not be guaranteed owing to inevitable communication delays or data interruptions. Bad data poses a risk to the robustness of data-driven methods, and existing literature have studied bad data identification methods [26], [27]. The consideration of bad data still needs to be addressed in the data-driven process. b) Conventional data-driven single-mode control may not satisfy the diverse operational requirements of ADNs in complex scenarios. In the control process, it is of significance to realize adaptive mode-switching and improve the operational performance according to the status of ADNs.

To address the above issues, this paper proposes a data-driven multi-mode adaptive control method for SOP with bad data, as shown in Fig. 1. Based on the robust HO-RLS method, a dynamic response function is established with real-time measurement data. Compared with conventional data-driven approaches, the robust HO-RLS method imposes a small computational burden and exhibits strong robustness against bad data. Furthermore, multiple modes can be adaptively switched to satisfy different operational requirements and improve the operational performance of ADNs. The HO-RLS method is first applied to the operation of SOP and is developed with multi-mode to realize data-driven adaptive control. The contributions of this paper are summarized as follows:

1) A data-driven framework for SOP operation is proposed based on HO-RLS, which depends on the measurement data rather than mechanism model. The linear response function between the SOP strategy and control target is established to respond to system state changes in complex scenarios. A bad data elimination approach is embedded into the response function for enhanced robustness based on the general iterative shrinkage and thresholding (GIST) method.

2) A multi-mode adaptive control strategy for SOP is proposed based on response function to improve operational performance, including voltage control, load balancing, economic operation, and mixed control modes. A dynamic triggering mechanism is designed to achieve adaptive mode switching based on state variation and measurements, which satisfies the diverse operational requirements.

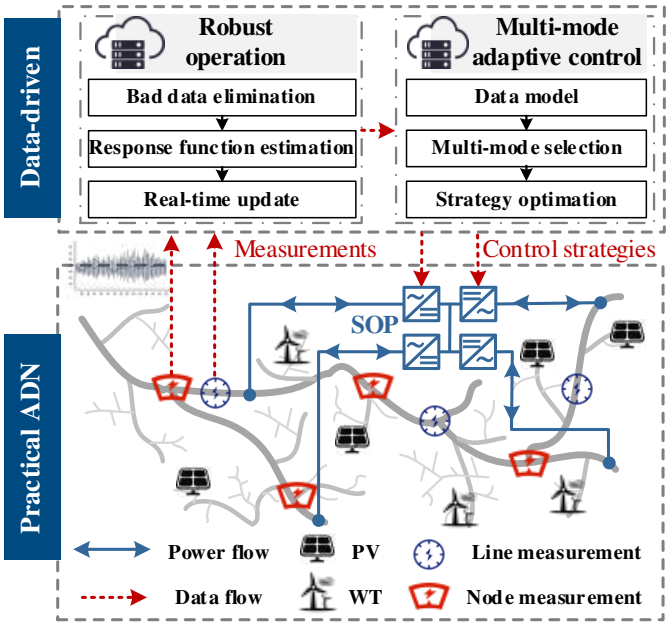


Fig. 1. The framework of proposed data-driven control.

The remainder of this paper is organized as follows. Section II introduces the data-driven operation of SOP based on the robust HO-RLS method. In Section III, a data-driven multi-mode adaptive control method is proposed. The case studies and analysis are presented in Section IV. Finally, the conclusions are drawn in Section V.

## II. Robust Data-driven Operation of SOP

Measurement quality has a significant impact on control performance. Considering bad data in measurements, a robust data-driven operation model of SOP is proposed based on the outlier-robust HO-RLS method. The linear response function between the SOP strategy and control target is established, which can dynamically describe the operational status and identify bad data.

### A. Data-driven Control of SOP

Consider an ADN with nodes denoted by the set $\mathcal{N} \coloneqq \{1,2,\dots,N\}$, lines denoted by the set $\mathcal{L} \coloneqq \{ij|i,j \in \mathcal{N}\}$, DGs denoted by the set $\mathcal{G} \coloneqq \{1,2,\dots,N_{\mathrm{DG}}\}$, and SOPs denoted by the set $\mathcal{S} \coloneqq \{1,2,\dots,N_{\mathrm{SOP}}\}$. The essence of data-driven operation of SOP is to establish the relationship between the objectives and SOP strategy. The nonlinear relation at time period $t$ can be formulated as follows.

$$\boldsymbol{y}_t = f_t(\boldsymbol{x}_t) \tag{1}$$

where $\boldsymbol{y}_t = \{\boldsymbol{y}_t^{\mathrm{U}}, \boldsymbol{y}_t^{\mathrm{L}}, \boldsymbol{y}_t^{\mathrm{P}}\} \in \mathbb{R}^M$ represents the measurement vector collected from the ADN at time period $t$, which can be the nodal voltage, line current, and line power measurements. $\boldsymbol{x}_t = \{\boldsymbol{x}_{t,n}^{\mathrm{SOP}} = \left[P_t^{\mathrm{SOP}}, Q_t^{\mathrm{SOP}}\right]_n | n \in \mathcal{S}\}$ represents the operational strategies of SOPs at time period $t$, including the active power transfer and reactive power support. $f_t$ describes the nonlinear relation between the measurement vector $\boldsymbol{y}_t$ and operational strategy $\boldsymbol{x}_t$, which is dependent on the system models, such as the line impedance and load levels.

Although the above equations are nonlinear, preliminary research has provided a linear approximation to realize real-time optimal power flow [28]. In addition, the nonlinear function $f_t$ in (1) relies on accurate network parameters, which are difficult to obtain in practice. Thus, a data-driven linearized response function of ADNs is constructed, as shown in (2).

$$\boldsymbol{y}_t = \boldsymbol{F}_t \cdot \boldsymbol{x}_t \tag{2}$$

where $\boldsymbol{F}_t$ is the linearized form of $f_t$. Our target is to estimate the response function $\boldsymbol{F}_t$ based on the measurement data of ADNs at time $t$.

### B. Estimation of Response Function

#### 1) Design of response function

Measuring errors and bad data are inevitable owing to the accuracy of measurement devices or communication delay. Thus, considering the measuring error and bad data, (2) is further extended to (3).

$$\tilde{\boldsymbol{y}}_t = \boldsymbol{F}_t' \cdot \boldsymbol{q}_t + \boldsymbol{o}_t + \boldsymbol{\varepsilon}_t \tag{3}$$

where $\boldsymbol{\varepsilon}_t \in \mathbb{R}^M$ is the measurement error, which can be generally assumed to be a Gaussian distribution [29]. $\boldsymbol{o}_t \in \mathbb{R}^M$ models the bad data with sparsity. $\boldsymbol{q}_t = [(\boldsymbol{x}_t)^{\mathrm{T}}, 1]^{\mathrm{T}} \in \mathbb{R}^M$ is the auxiliary optimization vector. $\boldsymbol{F}_t'$ is the practical response function to be estimated.

Considering diverse control objectives in the following section, four forms of response function $\boldsymbol{F}_t'$ are considered, which is described as follows.

$$\boldsymbol{F}_t' = \begin{bmatrix} \omega_t^{\mathrm{U}} \boldsymbol{F}_t'^{[\mathrm{U}]} \\ \omega_t^{\mathrm{L}} \boldsymbol{F}_t'^{[\mathrm{L}]} \\ \omega_t^{\mathrm{P}} \boldsymbol{F}_t'^{[\mathrm{P}]} \\ \omega_t^{\mathrm{M}} \boldsymbol{F}_t'^{[\mathrm{M}]} \end{bmatrix} \tag{4a}$$

$$\sum_{\{*\} \in \Omega_{\mathrm{O}}} \omega_t^{\{*\}} = 1, \omega_t^{\{*\}} \in \{0,1\} \tag{4b}$$

$$\Omega_{\mathrm{O}} = \{\mathrm{U}, \mathrm{L}, \mathrm{P}, \mathrm{M}\} \tag{4c}$$

where $\Omega_{\mathrm{O}}$ is the set of control mode. U, L, P, and M represent voltage control mode, load balancing mode, economic operation mode, and mixed control mode, respectively. The mode flag $\omega_t^{\{*\}}$ is assigned by the dynamic triggering mechanism based on measurements and the state variation. When a mode is

activated, the corresponding flag is assigned as 1. The detailed description on the modes will be introduced in Section III.

*2) Estimation of response function*

A typical estimation is to form a regularized least squares (RLS) estimator to solve the response function $\boldsymbol{F}'_t$ in real-time with the available data pair $(\tilde{\boldsymbol{y}}_t, \boldsymbol{q}_t)$. However, the computational burden will increase with large-scale systems. To address this issue, the robust HO-RLS method is introduced, which utilizes the recursions form to deal with bad data and simplify the calculation. The data-driven estimation of response function based on robust HO-RLS method is expressed as follows. For all $t > t_0$, it satisfies:

$$\hat{\boldsymbol{o}}_t \in \underset{\boldsymbol{o}}{\operatorname{argmin}} \frac{1}{2}||\tilde{\boldsymbol{y}}_t - \hat{\boldsymbol{F}}'_{t-1}\boldsymbol{q}_t - \boldsymbol{o}||^2 + \lambda_{\text{LASSO}}||\boldsymbol{o}||_1 \tag{5a}$$

$$\hat{\boldsymbol{F}}'_t = \text{HO-RLS}(\hat{\boldsymbol{F}}'_{t-1}, (\boldsymbol{q}_t, \tilde{\boldsymbol{y}}_t - \hat{\boldsymbol{o}}_t)) \tag{5b}$$

where $\lambda_{\text{LASSO}} > 0$ is the Least absolute shrinkage and selection operator (LASSO) regression coefficient. HO-RLS $(\hat{\boldsymbol{F}}'_{t-1}, (\boldsymbol{q}_t, \tilde{\boldsymbol{y}}_t - \hat{\boldsymbol{o}}_t))$ denotes the HO-RLS updates, with the newly obtained data $(\boldsymbol{q}_t, \tilde{\boldsymbol{y}}_t - \hat{\boldsymbol{o}}_t)$ at time period $t$. All four types of response function in (4) can be obtained according to measurement data and dynamically updated.

Two issues remain to be addressed, including initialization and dynamic update. As for initialization, the initial state is vital to the operation and control, which influences the optimal estimation of the response function, and further impact the convergence and control effect. If the proper initial values are selected, then the response function is obtained, and the further control can adaptively adjust the SOP strategies. In the control process, the physical constraints must always be satisfied within a reasonable range. Therefore, the initialization is realized offline with a fixed time window $t_0$, as shown in (6).

$$(\hat{\boldsymbol{F}}'_{t_0}, \{\hat{\boldsymbol{o}}_u\}_{u=1}^{t_0}) \in \underset{(\boldsymbol{F}, \{\boldsymbol{o}_u\}_{u=1}^{t_0})}{\operatorname{argmin}} \boldsymbol{\mathcal{F}} \tag{6a}$$

$$\boldsymbol{\mathcal{F}} = \sum_{u=1}^{t}[\frac{1}{2}||\tilde{\boldsymbol{y}}_u - \boldsymbol{F}\boldsymbol{q}_u - \boldsymbol{o}_u||^2 + \lambda_u \rho(\boldsymbol{o}_u)] \tag{6b}$$

As for the dynamic update, the sample-average loss is adopted to approximate the response function: $g_t(\boldsymbol{F}) = \frac{1}{2\Gamma_t}\sum_{p=t_0}^{t}\gamma^{t-p}||\tilde{\boldsymbol{y}}_p - \boldsymbol{F}\boldsymbol{q}_p - \boldsymbol{o}_p||^2$. $\gamma \in (0,1]$ is the forgetting factor that mimics the classical exponentially-weighted RLS and $\Gamma_t = \sum_{p=t_0}^{t}\gamma^{t-p}$.

The update of HO-RLS is based on the gradient of $g_t(\boldsymbol{F})$. For all $t > t_0$, define the correlation matrices $\boldsymbol{R}_{ab,t}$ as follows.

$$\boldsymbol{R}_{ab,t} = \frac{1}{\Gamma_t}\sum_{p=t_0}^{t}\gamma^{t-p}\,\boldsymbol{a}_p\boldsymbol{b}_p^{\mathrm{T}} \tag{7}$$

so that for the processes $\boldsymbol{q}_p$, $\tilde{\boldsymbol{y}}_p$, and $\boldsymbol{o}_p$ under study, define $\boldsymbol{R}_{qq,t}$, $\boldsymbol{R}_{\tilde{y}q,t}$, and $\boldsymbol{R}_{oq,t}$, respectively.

Then, the gradient of $l_t$ can be expressed as $\nabla g_t(\boldsymbol{F}) = (\hat{\boldsymbol{F}}'_{t-1}\boldsymbol{R}_{qq,t} - \boldsymbol{R}_{yq,t} + \boldsymbol{R}_{oq,t})$. The previous gradient information is incorporated into HO-RLS via the mapping $T_t(\boldsymbol{F}) = F - \frac{1}{\varpi_t}\nabla g_t(\boldsymbol{F})$ to produce the update process, which is formulated as follows.

$$\begin{aligned}\hat{\boldsymbol{F}}'_{t+\frac{1}{2}} = \hat{\boldsymbol{F}}'_{t-1} + \hat{\boldsymbol{F}}'_{t-\frac{1}{2}} - \hat{\boldsymbol{F}}'_{t-2} + \frac{\alpha}{\varpi_{t-1}}\big(\hat{\boldsymbol{F}}'_{t-2}\boldsymbol{R}_{qq,t-1} - \\ \boldsymbol{R}_{\tilde{y}q,t-1} + \boldsymbol{R}_{oq,t-1}\big) - \frac{1}{\varpi_t}\big(\hat{\boldsymbol{F}}'_{t-1}\boldsymbol{R}_{qq,t} - \boldsymbol{R}_{\tilde{y}q,t} + \boldsymbol{R}_{oq,t}\big)\end{aligned} \tag{8}$$

where $\varpi_t$ is to overestimate the spectral norm with the aid of user-defined $\varepsilon_\varpi > 0$. Since $\big(\hat{\boldsymbol{F}}'_{t-2}\boldsymbol{R}_{qq,t-1} - \boldsymbol{R}_{\tilde{y}q,t-1} + \boldsymbol{R}_{oq,t-1}\big)$ is already available in the last recursion, the computational burden can be reduced and the real-time performance is ensured.

*3) Robust estimation against bad data*

Owing to communication delays or data interruptions, the measuring data inevitably contains bad data [30], [31]. Data-driven approaches only rely on measurements to achieve the data model construction and solution without state estimation, which have high requirements for data quality. Thus, data-driven approaches should consider the impact of measuring bad data for enhanced robustness. Bad data elimination is embedded into the HO-RLS process based on GIST method [32]. The HO-RLS is based on steepest-descent directions with a constant step size, which does not require matrix inversion, and has low computational complexity. The theoretical analysis is provided in [24] for the convergence of HO-RLS solution. Bad data identification is processed as a subtask of HO-RLS and is regarded as a sparse optimization problem, as shown in (9).

$$\begin{aligned}&\underset{\boldsymbol{o}}{\operatorname{argmin}}\, h_t(\boldsymbol{o}) = l_t(\boldsymbol{o}) + r_t(\boldsymbol{o}) \\ &l_t(\boldsymbol{o}) = \tfrac{1}{2}||\tilde{\boldsymbol{y}}_t - \hat{\boldsymbol{F}}'_{t-1}\boldsymbol{q}_t - \boldsymbol{o}||^2 \\ &r_t(\boldsymbol{o}) = \lambda_{\text{LASSO}}||\boldsymbol{o}||_1\end{aligned} \tag{9}$$

The GIST-based bad data identification method solves problem (9) by generating a sequence $\{\boldsymbol{o}_k\}$ via:

$$\begin{aligned}\boldsymbol{o}_{k+1} = \underset{\boldsymbol{o}}{\operatorname{argmin}}\, l_t(\boldsymbol{o}_k) + < \nabla l_t(\boldsymbol{o}_k), \boldsymbol{o} - \boldsymbol{o}_k > \\ + \tfrac{\tau_k}{2}||\boldsymbol{o} - \boldsymbol{o}_k||^2 + r(o)\end{aligned} \tag{10}$$

In fact, problem (10) is equivalent to the following proximal operator problem:

$$\begin{aligned}&\boldsymbol{o}_{k+1} = \underset{\boldsymbol{o}}{\operatorname{argmin}} \tfrac{1}{2}||\boldsymbol{o} - \boldsymbol{w}_k(\boldsymbol{o}_k + \tfrac{1}{\tau_k})||^2 + \tfrac{1}{\tau_k}\lambda||\boldsymbol{o}||_1 \\ &\tau_{k+1} = \eta\tau_k\end{aligned} \tag{11}$$

where $\boldsymbol{w}_k = \boldsymbol{o}_k - \nabla l_t(\boldsymbol{o}_k)/\tau_k$. Thus, a gradient descent along the direction $-\nabla l_t(\boldsymbol{o}_k)$ with step size $\tau_k$ is first performed and is updated adaptively. Then, a proximal operator problem is solved.

At each iteration, the appropriate initial step size can significantly reduce the computational burden, which is crucial for algorithm convergence. Thus, at each iteration of the algorithm, a line search initialized by the Barzilai-Borwein rule is utilized to improve the computational efficiency, as shown in (12).

$$\begin{aligned}&\tau_k = \arg\min_t ||t\boldsymbol{a}_k - \boldsymbol{b}_k||^2 = \tfrac{<\boldsymbol{a}_k, \boldsymbol{b}_k>}{<\boldsymbol{a}_k, \boldsymbol{a}_k>} \\ &\boldsymbol{a}_k = \boldsymbol{o}_k - \boldsymbol{o}_{k-1},\ \boldsymbol{b}_k = \nabla h(\boldsymbol{o}_k) - \nabla h(\boldsymbol{o}_{k-1})\end{aligned} \tag{12}$$

One commonly used line search criterion is to require that the objective function is monotonically decreasing. Thus, the step size $1/\tau_k$ is accepted if the following monotone line search criterion is satisfied:

$$h_t(\boldsymbol{o}_{k+1}) \le h_t(\boldsymbol{o}_k) - \frac{\sigma}{2}\tau_k||\boldsymbol{o}_{k+1} - \boldsymbol{o}_k||^2 \tag{13}$$

where $\sigma$ is a constant in the interval $(0,1)$.

In summary, the process of robust estimation of data-driven response function is given in Algorithm 1.

**Algorithm 1:** Robust estimation of response function

**Data:** $(\boldsymbol{q}_t, \boldsymbol{y}_t)$

**User's input:** $t_0$, $\alpha \in (0.5,1]$, $\lambda \in \mathbb{R} > 0$, $\varepsilon_{\varpi} \in \mathbb{R} > 0$.

**Output:** Sequence $\boldsymbol{F}_t$, $t > t_0$

**Initialization**

$(\widehat{\boldsymbol{F}}'_t, \{\widehat{\boldsymbol{o}}_u\}_{u=1}^{t_0}) \in \underset{(\boldsymbol{F},\{\boldsymbol{o}_u\}_{u=1}^{t_0})}{\operatorname{argmin}} \mathcal{F}$

$\varpi_{t_0} = ||\boldsymbol{R}_{qq,t_0}|| + \varepsilon_{\varpi}$

$\widehat{\boldsymbol{F}}'_{t_0/2} = \widehat{\boldsymbol{F}}'_{t_0-1} - \frac{\alpha}{\varpi_{t_0}}(\widehat{\boldsymbol{F}}'_{t_0-1}\boldsymbol{R}_{qq,t_0} - \boldsymbol{R}_{\tilde{y}q,t_0} + \boldsymbol{R}_{oq,t_0})$

$\widehat{\boldsymbol{F}}'_{t_0} = \widehat{\boldsymbol{F}}'_{t_0/2}$

**end**

**for** $t = t_0 + 1$ **to** $+\infty$ **do**

$\widehat{\boldsymbol{o}}_t \in \underset{\boldsymbol{o}}{\operatorname{argmin}} \frac{1}{2}||\tilde{\boldsymbol{y}}_t - \widehat{\boldsymbol{F}}'_{t-1}\boldsymbol{q}_t - \boldsymbol{o}||^2 + \lambda_{\mathrm{LASSO}}||\boldsymbol{o}||_1$

$\boldsymbol{q}_t = \boldsymbol{R}_{qq,t}\boldsymbol{p}_{t-1}$; $\boldsymbol{p}_t = \boldsymbol{q}_t/||\boldsymbol{q}_t||$

$\varpi_t = \boldsymbol{p}_t^{\mathrm{T}}\boldsymbol{R}_{qq,t}\boldsymbol{p}_t + \varepsilon_{\varpi}$

$\widehat{\boldsymbol{F}}'_{\frac{t}{2}} = \widehat{\boldsymbol{F}}'_{t-1} + \widehat{\boldsymbol{F}}'_{\frac{t-2}{2}} - \widehat{\boldsymbol{F}}'_{t-2} + \frac{\alpha}{\varpi_{t-1}}(\widehat{\boldsymbol{F}}'_{t-2}\boldsymbol{R}_{qq,t-1} - \boldsymbol{R}_{\tilde{y}q,t-1} + \boldsymbol{R}_{oq,t-1}) - \frac{1}{\varpi_t}(\widehat{\boldsymbol{F}}'_{t-1}\boldsymbol{R}_{qq,t} - \boldsymbol{R}_{\tilde{y}q,t} + \boldsymbol{R}_{oq,t})$

$\widehat{\boldsymbol{F}}'_t = \widehat{\boldsymbol{F}}'_{t/2}$

**end**

The response function is obtained based on the robust HO-RLS method while enhancing the robustness against bad data, which can provide effective guidance information for data-driven control.

## III. Multi-mode Adaptive Control for SOP

Conventional single-mode regulation of SOP may not meet the diverse operational requirements of ADNs in complex environments. Based on the response functions estimated in the previous section, this part constructs the multi-mode adaptive control strategy for SOP. With the real-time measurement data, different modes can be adaptively switched and the operational strategies of SOP can be adjusted to improve the performance and realize the flexible operation of ADNs.

### A. Principle of Multi-Mode Control

To meet different operational requirements, four modes are formulated, as shown in Fig. 2. Modes I, II, III, and IV represent voltage control, load balancing, economic operation, and mixed control modes, respectively. It is assumed that SOP is operated in one mode at any period. Then, a dynamic triggering mechanism is designed to achieve mode switching adaptively based on measurements and the state variation. The mode flags for different modes are shown in (14).

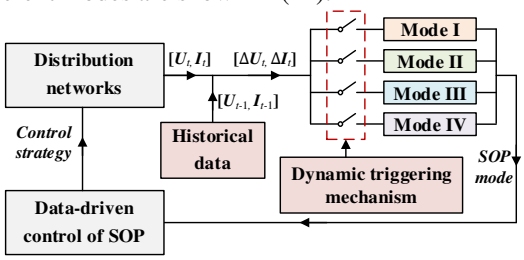


Fig. 2. Four operation modes of SOP.

$$\begin{cases} \omega_t^{\mathrm{U}} = 1, & \text{if condition C1 is satisfied} \\ \omega_t^{\mathrm{L}} = 1, & \text{if condition C2 is satisfied} \\ \omega_t^{\mathrm{P}} = 1, & \text{if condition C3 is satisfied} \\ \omega_t^{\mathrm{M}} = 1, & \text{if condition C4 is satisfied} \end{cases} \tag{14a}$$

$$\begin{cases} \text{C1: } \boldsymbol{U}_t \notin [\boldsymbol{U}_{\min}, \boldsymbol{U}_{\max}] \ \&\ C_{\mathrm{U}} > \sigma_{\mathrm{U}} \\ \text{C2: } \boldsymbol{I}_t \notin [0, \boldsymbol{I}^{\mathrm{thr}}] \ \&\ C_{\mathrm{L}} > \sigma_{\mathrm{L}} \\ \text{C3: } \boldsymbol{U}_t \in [\boldsymbol{U}_{\min}, \boldsymbol{U}_{\max}] \ \&\ \boldsymbol{I}_t \in [0, \boldsymbol{I}^{\mathrm{thr}}] \\ \text{C4: } \boldsymbol{U}_t \notin [\boldsymbol{U}_{\min}, \boldsymbol{U}_{\max}] \ \&\ \boldsymbol{I}_t \notin [0, \boldsymbol{I}^{\mathrm{thr}}] \end{cases} \tag{14b}$$

where $\omega_t^{\mathrm{U}} = 1$ indicates that Mode I is activated, the same meaning for $\omega_t^{\mathrm{L}}$, $\omega_t^{\mathrm{P}}$, and $\omega_t^{\mathrm{M}}$. $\sigma_{\mathrm{U}}$ and $\sigma_{\mathrm{L}}$ are the thresholds for voltage deviation and current loading deviation, respectively. $C_{\mathrm{U}}$ and $C_{\mathrm{L}}$ represent voltage deviation cost and current loading deviation cost of state variation between periods $t$ and $t-1$, respectively. Taking $C_{\mathrm{U}}$ as an example, $C_{\mathrm{U}} = \sum_{i\in\mathcal{N}} \Delta U_{i,t} P_{i,t}$, where the voltage changes between $\boldsymbol{U}_t$ and $\boldsymbol{U}_{t-1}$ is converted into the cost of voltage deviation [33]. $C_{\mathrm{L}}$ can be obtained in the similar way.

### B. Multi-mode Adaptive Control Model

*1) Mode I: voltage control mode*

This mode minimizes the voltage deviation and maintains it within a reasonable range by the flexible control of SOP. Therefore, the active power and reactive power of the SOP in Mode I are determined by minimum voltage deviation cost. The data model of Mode I is formulated as follows.

$$\boldsymbol{U}_t = \widehat{\boldsymbol{F}}_t^{\prime[\mathrm{U}]}\boldsymbol{q}_t \tag{15a}$$

$$\tilde{\boldsymbol{y}}_t^{\mathrm{U}} = \boldsymbol{U}_t + \boldsymbol{o}_t + \boldsymbol{\varepsilon}_t \tag{15b}$$

where $\widehat{\boldsymbol{F}}_t^{\prime[\mathrm{U}]}$ is the response function of Mode I, which is calculated by Algorithm 1.

The objective function of Mode I is described as (16).

$$\min J_1 = \left(\boldsymbol{y}^{\mathrm{U,ref}} - \tilde{\boldsymbol{y}}_t^{\mathrm{U}}\right)^{\mathrm{T}}\left(\boldsymbol{y}^{\mathrm{U,ref}} - \tilde{\boldsymbol{y}}_t^{\mathrm{U}}\right) + \lambda||\boldsymbol{q} - \boldsymbol{q}_{t-1}||^2 \tag{16}$$

where $\boldsymbol{y}^{\mathrm{U,ref}}$ is the nodal voltage reference, which is usually takes a value of $\mathbf{1}$.

*2) Mode II: load balancing mode*

Each feeder of ADNs consists of different types of loads, such as industrial, commercial, and residential loads. The integration of DGs exacerbates the load imbalance, leading to the inefficient use of network assets. Therefore, this mode is designed to balance the load between the feeders and improve the efficiency of the ADN. The data model of Mode II is formulated as follows.

$$\left(\frac{\boldsymbol{I}_t}{\boldsymbol{I}_{\max}}\right)^2 = \widehat{\boldsymbol{F}}_t^{\prime[\mathrm{L}]}\boldsymbol{q}_t \tag{17a}$$

$$\tilde{\boldsymbol{y}}_t^{\mathrm{L}} = \left(\frac{\boldsymbol{I}_t}{\boldsymbol{I}_{\max}}\right)^2 + \boldsymbol{o}_t + \boldsymbol{\varepsilon}_t \tag{17b}$$

where $\widehat{\boldsymbol{F}}_t^{\prime[\mathrm{L}]}$ is the response function of Mode II, which can be also obtained by Algorithm 1.

The objective function of Mode II is described as (18).

$$\min J_2 = \left(\boldsymbol{y}^{\mathrm{L,ref}} - \tilde{\boldsymbol{y}}_t^{\mathrm{L}}\right)^{\mathrm{T}}\left(\boldsymbol{y}^{\mathrm{L,ref}} - \tilde{\boldsymbol{y}}_t^{\mathrm{L}}\right) + \lambda||\boldsymbol{q} - \boldsymbol{q}_{t-1}||^2 \tag{18}$$

where $\boldsymbol{y}^{\mathrm{L,ref}}$ is the current loading reference, which is based on historical data and operating experience.

*3) Mode III: economic operation mode*

The optimal operation point changes with the fluctuation of the DGs, loads, and other devices. Mode III is designed to

reduce network loss with a reasonable voltage range and current loading level. Owing to the quadratic relationship between the power and line current, the square of line current is utilized to describe the network loss. The data model of Mode III is formulated as follows.

$$\boldsymbol{I}_t^2 = \widehat{\boldsymbol{F}}_t'^{[\mathrm{P}]}\boldsymbol{q}_t \tag{19a}$$

$$\widetilde{\boldsymbol{y}}_t^{\mathrm{P}} = \boldsymbol{I}_t^2 + \boldsymbol{o}_t + \boldsymbol{\varepsilon}_t \tag{19b}$$

where $\widehat{\boldsymbol{F}}_t'^{[\mathrm{P}]}$ is the response function of Mode III calculated by Algorithm 1.

The objective function of Mode III is described as follows.

$$\min J_3 = \left(\boldsymbol{y}^{\mathrm{P,ref}} - \widetilde{\boldsymbol{y}}_t^{\mathrm{P}}\right)^{\mathrm{T}}\left(\boldsymbol{y}^{\mathrm{P,ref}} - \widetilde{\boldsymbol{y}}_t^{\mathrm{P}}\right) + \lambda||\boldsymbol{q} - \boldsymbol{q}_{t-1}||^2 \tag{20}$$

*4) Mode IV: mixed control mode*

In practice, voltage violation and load imbalance may occur at the same time. Based on Modes I and II, the mixed control mode is designed as (21).

$$\boldsymbol{M}_t = \widehat{\boldsymbol{F}}_t'^{[\mathrm{M}]}\boldsymbol{q}_t \tag{21a}$$

$$\widetilde{\boldsymbol{y}}_t^{\mathrm{M}} = \boldsymbol{M}_t + \boldsymbol{o}_t + \boldsymbol{\varepsilon}_t \tag{21b}$$

$$\widetilde{\boldsymbol{y}}_t^{\mathrm{M}} = [\widetilde{\boldsymbol{y}}_{t,1}^{\mathrm{M}}, \widetilde{\boldsymbol{y}}_{t,2}^{\mathrm{M}}] \tag{21c}$$

$$\boldsymbol{M}_t = \left[\boldsymbol{U}_t; \left(\frac{\boldsymbol{I}_t}{\boldsymbol{I}_{\max}}\right)^2\right] \tag{21d}$$

$$\widehat{\boldsymbol{F}}_t'^{[\mathrm{M}]} = \left[\widehat{\boldsymbol{F}}_{t,1}'^{[\mathrm{M}]}; \widehat{\boldsymbol{F}}_{t,2}'^{[\mathrm{M}]}\right] \tag{21e}$$

where $\widehat{\boldsymbol{F}}_t'^{[\mathrm{M}]}$ is the response function of Mode IV. $\boldsymbol{M}_t$ includes voltage measurement and line current measurement.

The objective function of Mode IV is described as follows.

$$\begin{aligned}\min J_4 = {} & \mu_{1,t}\left(\boldsymbol{y}^{\mathrm{U,ref}} - \widetilde{\boldsymbol{y}}_{t,1}^{\mathrm{M}}\right)^{\mathrm{T}}\left(\boldsymbol{y}^{\mathrm{U,ref}} - \widetilde{\boldsymbol{y}}_{t,1}^{\mathrm{M}}\right) + \\ & \mu_{2,t}\left(\boldsymbol{y}^{\mathrm{L,ref}} - \widetilde{\boldsymbol{y}}_{t,2}^{\mathrm{M}}\right)^{\mathrm{T}}\left(\boldsymbol{y}^{\mathrm{L,ref}} - \widetilde{\boldsymbol{y}}_{t,2}^{\mathrm{M}}\right) + \lambda||\boldsymbol{q} - \boldsymbol{q}_{t-1}||^2\end{aligned} \tag{22}$$

where $\mu_{1,t}$ and $\mu_{2,t}$ are weight coefficient, which represents the penalty coefficient for voltage violations and current loading violations and can be calculated as follows.

$$\xi_{i,t}^{\mathrm{U}} = \begin{cases} 0, & U_{\min,i}^{\mathrm{thr}} \le U_{i,t} \le U_{\max,i}^{\mathrm{thr}} \\ \dfrac{U_{\min,i}^{\mathrm{thr}} - U_{i,t}}{U_{\min,i}^{\mathrm{thr}} - U_{\min,i}}, & U_{\min,i} < U_{i,t} \le U_{\min,i}^{\mathrm{thr}} \\ \dfrac{U_{i,t} - U_{\max,i}^{\mathrm{thr}}}{U_{\max,i} - U_{\max,i}^{\mathrm{thr}}}, & U_{\max,i}^{\mathrm{thr}} < U_{i,t} \le U_{\max,i} \\ 1, & U_{i,t} < U_{\min,i}, U_{i,t} > U_{\max,i} \end{cases} \tag{23a}$$

$$\xi_{ij,t}^{\mathrm{I}} = \begin{cases} 0, & 0 < I_{ij,t}^2 \le \left(I_{ij,t}^{\mathrm{thr}}\right)^2 \\ \dfrac{I_{ij,t}^2 - \left(I_{ij,t}^{\mathrm{thr}}\right)^2}{\left(I_{ij,t}^{\max}\right)^2 - \left(I_{ij,t}^{\mathrm{thr}}\right)^2}, & \left(I_{ij,t}^{\mathrm{thr}}\right)^2 < I_{ij,t}^2 \le \left(I_{ij,t}^{\max}\right)^2 \\ 1, & \left(I_{ij,t}^{\max}\right)^2 < I_{ij,t}^2 \end{cases} \tag{23b}$$

$$\mu_{1,t} = \frac{\sum_{i\in\mathcal{N}} \xi_{i,t}^{\mathrm{U}}}{\sum_{i\in\mathcal{N}} \xi_{i,t}^{\mathrm{U}} + \sum_{ij\in\mathcal{L}} \xi_{ij,t}^{\mathrm{I}}} \tag{23c}$$

$$\mu_{2,t} = \frac{\sum_{ij\in\mathcal{L}} \xi_{ij,t}^{\mathrm{I}}}{\sum_{i\in\mathcal{N}} \xi_{i,t}^{\mathrm{U}} + \sum_{ij\in\mathcal{L}} \xi_{ij,t}^{\mathrm{I}}} \tag{23d}$$

where (23a) - (23b) represent the penalty coefficient of voltage violations and current loading violations, respectively. By calculating the penalty coefficient, the weight coefficient of the objective function can be determined to ensure effective solution for both voltage violations and current loading violations.

*5) Multi-mode adaptive control for SOP*

The multi-mode adaptive control model for SOP is summarized as follows.

$$\min J = f(\boldsymbol{q}_t) \tag{24a}$$

$$\text{s.t. } h(\boldsymbol{q}, \widetilde{\boldsymbol{y}}_t) \le 0 \tag{24b}$$

$$\widetilde{\boldsymbol{y}}_t = \widehat{\boldsymbol{F}}_t'\boldsymbol{q} + \boldsymbol{o}_t \tag{24c}$$

where (24a) represents objective function, which can be expressed as follows.

$$f(\boldsymbol{q}_t) = \omega_t^{\mathrm{U}} J_1 + \omega_t^{\mathrm{L}} J_2 + \omega_t^{\mathrm{P}} J_3 + \omega_t^{\mathrm{M}} J_4 \tag{25}$$

Unlike the linear weighted objective function, (25) indicates that only one mode can be activated at time $t$. (24b) represents the SOP operational constraints. The structure of an SOP is based on the power electronic device, which often adopts back-to-back voltage source converters. Taking an M-terminal SOP as an example, the operational constraints are formulated as follows.

$$\sum_{i\in\Omega_{\mathrm{m}}}^{M}\left(P_{t,i}^{\mathrm{SOP}} + P_{t,i}^{\mathrm{SOP,L}}\right) = 0 \tag{26a}$$

$$P_{t,i}^{\mathrm{SOP,L}} = A_i^{\mathrm{SOP}}\sqrt{\left(P_{t,i}^{\mathrm{SOP}}\right)^2 + \left(Q_{t,i}^{\mathrm{SOP}}\right)^2}, \forall i \in \Omega_{\mathrm{m}} \tag{26b}$$

$$Q_i^{\mathrm{SOP,min}} \le Q_{t,i}^{\mathrm{SOP}} \le Q_i^{\mathrm{SOP,max}}, \forall i \in \Omega_{\mathrm{m}} \tag{26c}$$

$$\sqrt{(P_{t,i}^{\mathrm{SOP}})^2 + (Q_{t,i}^{\mathrm{SOP}})^2} \le S_i^{\mathrm{SOP}}, \forall i \in \Omega_{\mathrm{m}} \tag{26d}$$

where constraints (26a) - (26c) represent the active and reactive power limits of multi-terminal SOP, respectively. Constraint (26d) represents the capacity limits of multi-terminal SOP.

Compared with other data-driven methods, the proposed multi-mode adaptive control method has several advantages. i) The response function contains system status information and is adaptively updated during the iterative process, which can provide correct guidance for control. ii) The objective function is scalable and can integrate diverse operation objectives to satisfy the diverse needs of ADN.

### C. Coordination and Transition among Different Modes

A dynamic triggering mechanism is designed to achieve mode switching adaptively. Three aspects are considered to improve the control performance. Measurements are utilized to determine whether the system state violates the secure operational constraints. The cost of state variation is considered to avoid frequent triggering of mode switching. The change of SOP output is added to the objective function to mitigate the impact on the system during mode switching.

Fig. 3 shows the coordination and transition among different modes. The operational mode of SOP is initialized as Mode III to reduce the network loss and improve the economy of ADN, which means $\omega_t^{\mathrm{P}} = 1$. Twelve switching conditions can activate the mode transition process. Due to the consideration of state variation, the operational mode can not be transmitted frequently. Specifically, if the voltage violation occurs and voltage variation exceeds the threshold, condition C1 is satisfied, and Mode I will be activated and take effect until the violation situation is alleviated. Taking mode transition with the sequence of Modes III-IV-I-III as an example, the operational mode is first in Mode III. When the voltage and current

loading violations occur simultaneously, the operational mode of SOP is switched to Mode IV. If after SOP regulation, the voltage still exceeds the threshold owing to DG fluctuations, the operational mode switches to Mode I. Until the violation situation is alleviated, Mode III is activated again. Thus, different modes can be adaptively switched and the operational strategies of SOP can be adjusted to realize the flexible operation of ADNs.

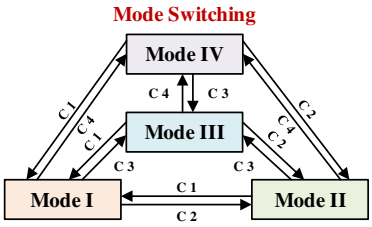


Fig. 3 Coordination and transition among different modes.

### D. Implementation of Data-driven Strategy of SOP

The flow chart of the proposed method is shown in Fig. 4. First, determine the operational mode of SOP based on the current system status. On the control time scale, by using the real-time measurement data, the data-driven operation model of SOP is established, which accurately estimates the response function. Then the multi-mode adaptive control for SOP is implemented to satisfy the operational requirements of ADN.

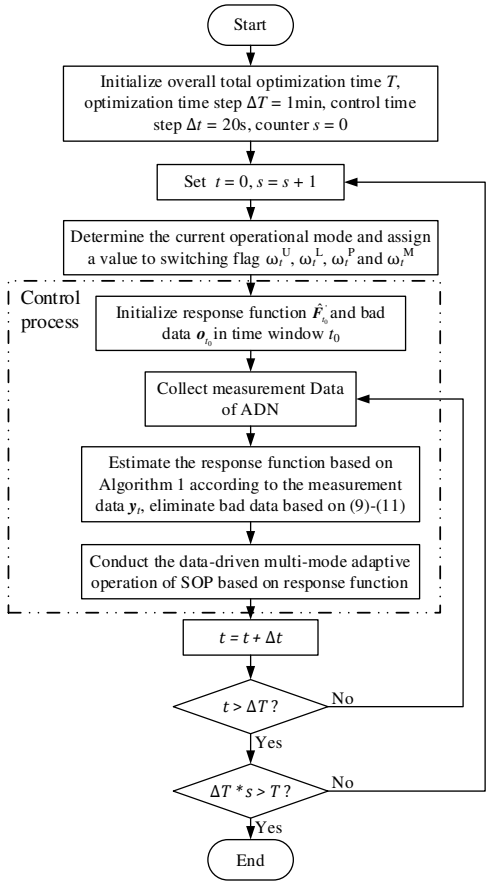


Fig. 4. Flow chart of data-driven multi-mode adaptive control method.

In summary, by establishing robust data-driven multi-mode adaptive operation of SOP, bad data can be addressed and the operational requirements can be effectively satisfied.

## IV. Case Studies and Analysis

In this section, the effectiveness of the proposed method for SOP is verified on a practical distribution network. The proposed method is implemented in the YALMIP optimization toolbox [34] with MATLAB R2020a and solved by Gurobi 10.0.1. All numerical experiments are carried out on an Intel Core i7 @ 3.20GHz computer with 16GB RAM.

### A. Distribution Networks with Four-terminal SOP

The structure of a practical distribution network is shown in Fig. 5. The system consists of three substations, of which the rated voltage level is 10.5 kV. The total active and reactive power demands are 9.99 MW and 7.34 Mvar, respectively [35]. To consider the impact of the high penetration of DGs, three photovoltaics (PVs) and three wind turbines (WTs) are integrated into the system, whose active power reaches almost 100% of the peak demand. The parameters of the DG capacity are listed in Table I. The capacity of each converter of multi-terminal SOP is set to 3.0 MVA.

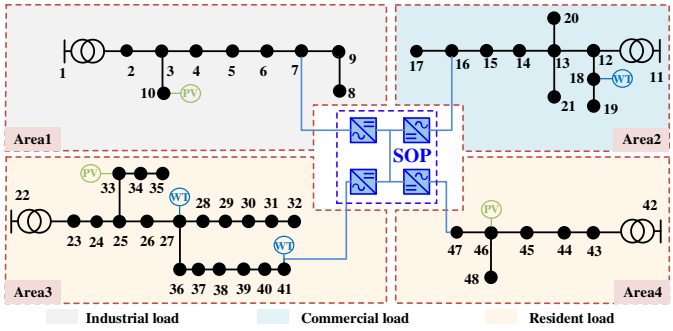


Fig. 5. Structure of practical distribution network.

TABLE I
PARAMETER OF DG INVERTER

| Type | PV | PV | PV | WT | WT | WT |
|---|---|---|---|---|---|---|
| Location | 10 | 33 | 46 | 18 | 27 | 41 |
| Capacity (kVA) | 1000 | 1000 | 1000 | 2000 | 2000 | 2000 |

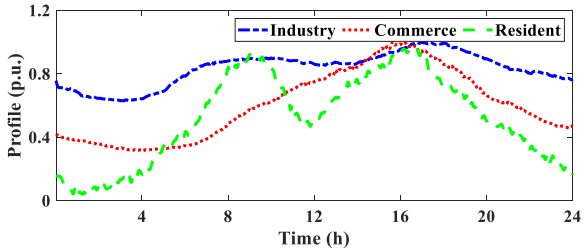


(a) Operation curves of loads.

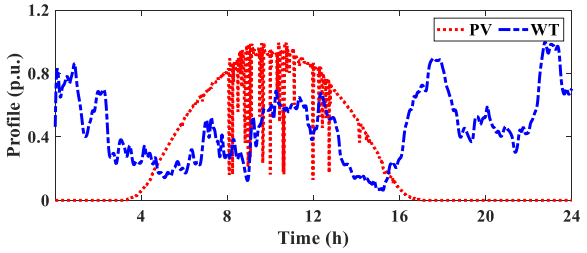


(b) Operation curves of DGs.

Fig. 6. Operation curves of DGs and loads.

Fig. 6 shows the daily operation curves of the DGs and loads, with a 1-minute time interval. The measurements are configured based on the area of SOP adjustment. The measurements are generated by adding the random measurement noise with Gaussian distribution to the real value. The maximum and minimum limits of the voltage range are set as 1.05 p.u. and 0.95 p.u., respectively. The maximum current loading is set as 0.5 p.u. The total optimization time $T$ is set as 24 hours. The optimization horizon $\Delta T$ is set as 1 minutes and the control horizon $\Delta t$ is set as 20 seconds, which is also adopted as the sampling time interval of the SCADA measurements. The convergence threshold $\varepsilon$ is set as 0.01.

## B. *Analysis of Multi-mode Control*

To fully consider the uncertainty of DGs and verify the control effect of the proposed method, four scenarios are considered.

Scenario I: The initial operation state of ADN is obtained without the SOP operation.

Scenario II: The proposed data-driven multi-mode adaptive control method of SOP is conducted.

Scenario III: The model-based day-ahead operation method of SOP is conducted.

Scenario IV: The model-based real-time operation method of SOP is conducted.

In Scenario III, the commonly used day-ahead operation strategy of SOP is obtained based on a day-ahead forecast curve of source and loads with a 15-minute time interval. In Scenario IV, the optimal value is obtained by real-time optimization based on the mechanism model. However, this method is difficult to implement in real-time control due to the huge computational and communication burden, so it is only the theoretical optimal value.

*1) Analysis of mode switching*

Fig. 7 shows the control mode-switching of the day, in which the black, dark grey, light gray, and white grids represent the voltage control mode (Mode I), load balancing mode (Mode II), economic operation mode (Mode III), and mixed control mode (Mode IV), respectively. It can be seen that the mode can be adaptively switched among the four modes. Specifically, voltage violation occurs from 0:00 to 1:10. The operation mode is switched to Mode I, which adjusts the voltage to the desired range. Then, the operation mode is switched to Mode III. Therefore, multi-mode adaptive control can rationally utilize control resources to realize the flexible operation of ADN.

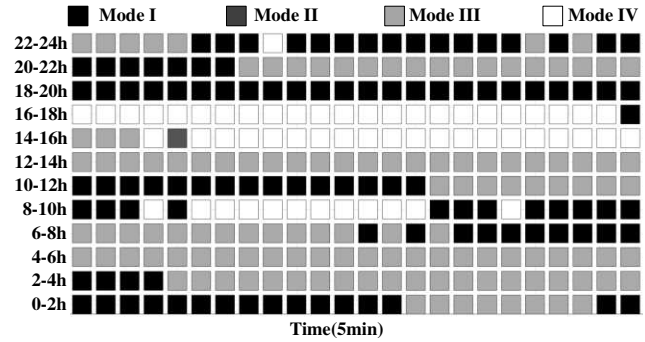


Fig. 7. Switching of different control modes in a day.

*2) Analysis of operation result*

Fig. 8 shows the voltage profiles in 24 hours. During 0:00-2:00 and 10:00-13:00, the voltage exceeds the upper limit due to the high active power outputs of WTs and PVs, respectively. The voltage exceeds the lower limit due to the heavy load during 18:00-22:00. Compared to Scenario I, the proposed method is conducted based on the accurate response function to maintain the voltage within a desired range. Fig. 9 shows the comparison of the voltage profile at node 7. Compared to the model-based day-ahead control in Scenario III, the proposed method can quickly respond to DG fluctuations, which also reduces the impact on ADN. However, the control effect cannot reach the optimal value in Scenario IV. The reason is that data-driven methods lack accurate model parameters and effective information from physical models.

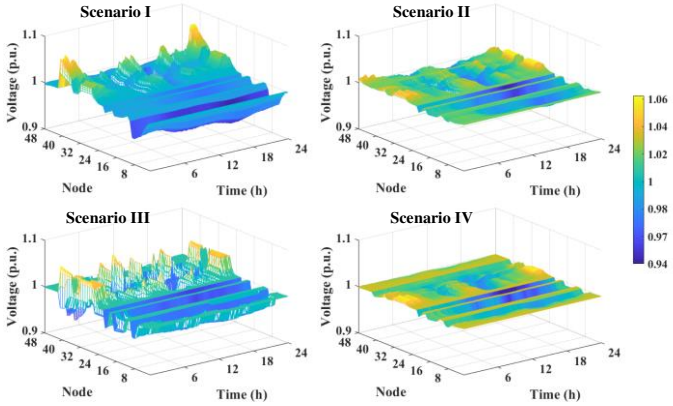


Fig. 8. Nodal voltage profiles in the test day.

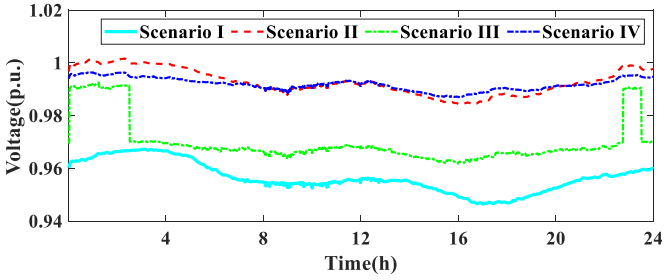


Fig. 9. Comparison of voltage profile at node 7.

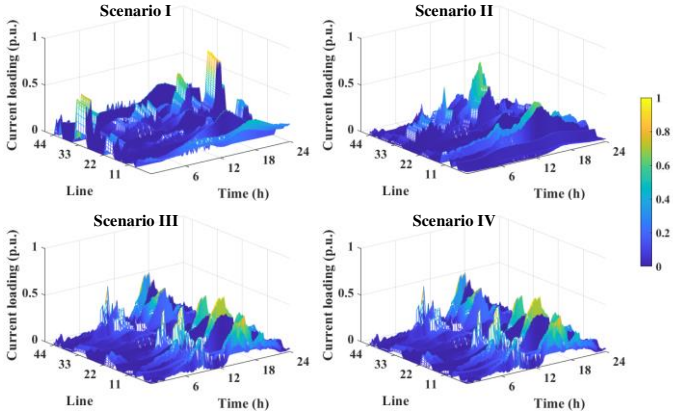


Fig. 10. Current loading in the test day.

Fig. 10 shows the current loading in 24 hours. The high current loading scenario mainly occurs in Areas 1 and 3.

Compared to Scenario I, the current loading in Scenario II is significantly reduced and comes close to the control effect with the optimal value in Scenario IV. Simultaneously, the nodal voltages remain within the desired range, which demonstrates the effectiveness of the proposed method.

Fig. 11 shows the network power loss in 24 hours. It can be seen that the network power loss in Scenario II is significantly reduced compared to Scenario I, which meets the economic operation requirements of ADN.

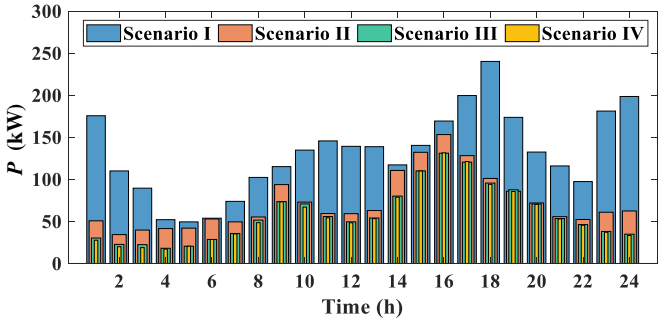


Fig. 11. Network power loss in the test day.

To quantify the control effect, voltage deviation index ($VDI$) and load balance index ($LBI$) are defined as (27).

$$VDI = \sum_{s\in T}\sum_{i\in \mathcal{N}}\left|y_i^{\mathrm{U,ref}} - U_i[s]\right|/(N * N_T) \tag{27a}$$

$$LBI = \sum_{s\in T}\sum_{j\in \mathcal{L}}\left|y_i^{\mathrm{M,ref}} - M_i[s]\right|/(N_n) \tag{27b}$$

The daily operation results of the four scenarios are shown in Table II. Compared to Scenario I, the proposed data-driven multi-mode operation strategy of SOP in Scenario II can effectively mitigate the voltage deviation and load imbalance of ADN. The voltage deviation, current loading, and power loss are reduced by 48.53%, 34.98%, and 47.13%, respectively. Compared to Scenario III, the proposed method has a significant improvement in voltage control, which can effectively address the impact of DG uncertainty. The optimal method in Scenario IV can achieve the best control effect, as the optimal solution can be obtained based on accurate model parameters.

TABLE II

OPERATION RESULT OF THE FOUR SCENARIOS

| Scenario | Minimum voltage (p.u.) | Maximum voltage (p.u.) | $VDI$ (p.u.) | $LBI$ (p.u.) | Power loss (kW) |
|---|---|---|---|---|---|
| I | 0.9409 | 1.0734 | 0.0068 | 58.2631 | 131.1204 |
| II | 0.9671 | 1.0175 | 0.0035 | 37.8854 | 69.3206 |
| III | 0.9340 | 1.0572 | 0.0064 | 39.0622 | 74.4027 |
| IV | 0.9701 | 1.0098 | 0.0021 | 27.0510 | 57.2022 |

### C. Convergence Analysis

The iterative data-driven method will inevitably affect the operation of the ADN owing to the interaction with the practical ADN in real time. Therefore, the data-driven method must achieve convergence within a limited number of iterations to reduce the impact on the real ADN. Taking 19:00 as an example, the proposed data-driven control effect and dynamic control process are shown in Fig. 12. The blue solid line represents the voltage profile without control in Scenario I. The red dotted line represents the voltage profile after the control in Scenario II. And the gray area represents the dynamic voltage control process in Scenario II.

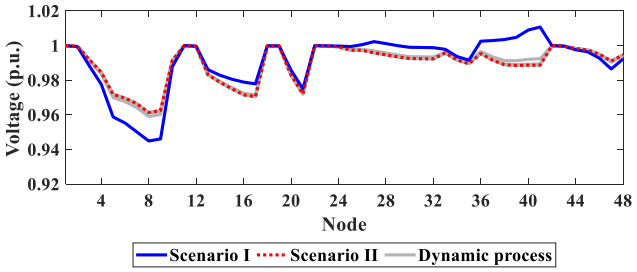


Fig. 12. Voltage profiles of control process at 19:00.

It can be seen from Fig. 12 that the accurate response function can effectively guide the SOP output, thus maintaining the voltages at a desired range. The computational efficiency of control process is shown in Table III. The computational efficiency of the control process is determined by the calculation time in each iteration and the number of iterations. The proposed method ensures convergence within the finite number of iterations, which also proves the effectiveness of the control strategy. In addition, the response function only needs to be calculated by a simple algebraic operation, bringing a small computational burden. The calculation time for each step is much less than the control horizon. Therefore, the control strategy can be completed to ensure real-time performance.

Fig. 13 shows the voltage iteration of nodes 8 and 38 at 19:00. Fig. 14 shows the operation strategy of SOP at 19:00. The residual meets the convergence threshold and can achieve rapid convergence benefitting from the accurate guidance of the response function.

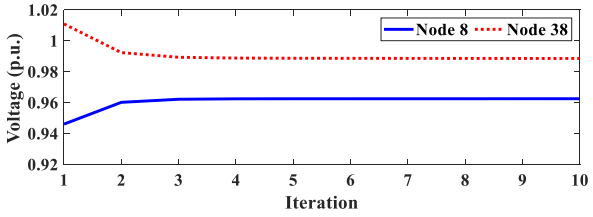


(a) Voltage iteration of nodes 8 and 38.

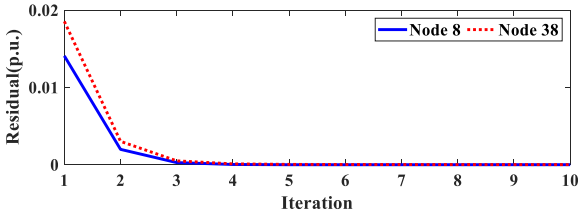


(b) Convergence of the residual of nodes 8 and 38.

Fig. 13. Voltage iteration at 19:00.

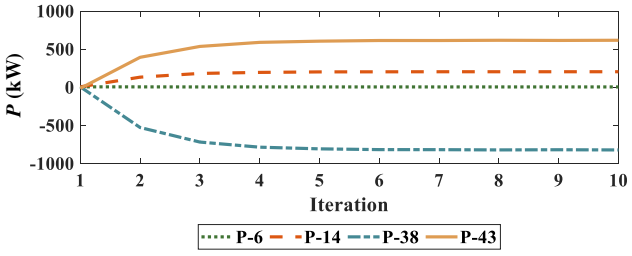


(a) Active power transfer of SOP.

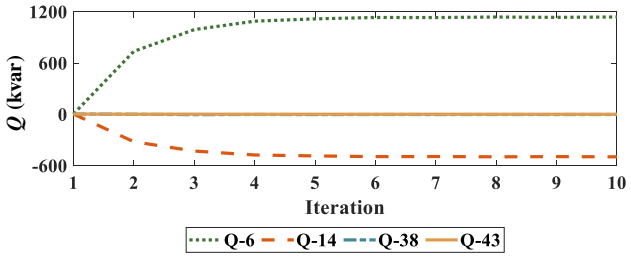


(b) Reactive power output of SOP.

Fig. 14. Operation strategy of SOP at 19:00.

The proposed method is compared with the mode free adaptive control (MFAC)-based method for SOP operation in [21]. Scenario V is added as follows.

Scenario V: The MFAC-based method of SOP is conducted.

The comparison is made by the number of convergence and computational time. Taking 19:00 as an example, the voltage control performances of Scenarios II and V are shown in Fig. 15. It can be seen that the MFAC method in Scenario V (blue line) converges after ten iterations, whereas the proposed method in Scenario II (red line) converges after only four iterations. This improves the convergence speed and ensures the real-time performance. In addition, the control effect of the two methods is almost at the same level, which further verifies the control effectiveness. The computational efficiency of control process is shown in Table III. Compared to the MFAC method, the proposed method has a higher computational speed. The average computational time in each iteration has been reduced from 0.5051s to 0.4286s. Due to a decrease in the number of convergences, the total computational time has been reduced from 5.0503s to 1.7145s.

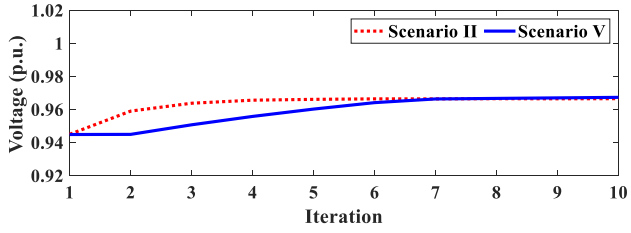


(a) Voltage iteration of node 8 at 19:00.

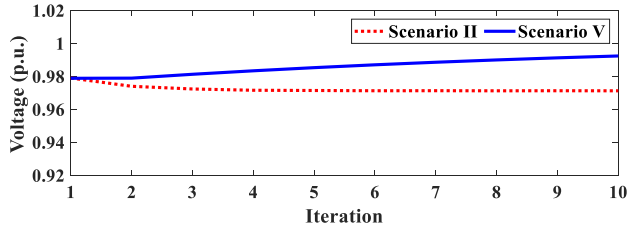


(b) Voltage iteration of node 16 at 19:00.

Fig. 15 Comparison of voltage control performances of Scenarios II and V.

TABLE III

COMPUTATIONAL EFFICIENCY OF CONTROL PROCESS

| Scenario | Number of convergence steps | Average computational time in each iteration (second) | Total computational time (second) |
|---|---|---|---|
| II | 4 | 0.4286 | 1.7145 |
| V | 10 | 0.5051 | 5.0503 |

Accurate guidance information has a significant impact on convergence performance. In the MFAC process, a feedback error mechanism is added to the data-driven operational control. The feedback error between measurement and the desired control objective in each iteration is utilized for correction. The correction performance will gradually decrease as the number of iterations increases, which leads to a reduction in convergence speed. In contrast, in addition to feedback errors, the proposed method can adaptively update the response function during the iteration process. The accurate response function contains the system operational situation information, which can provide effective guidance for the data-driven process. Therefore, the proposed data-driven method can realize state perception of the system and improve the control performance.

### *D. Robustness Analysis*

This subsection verifies the robustness of the proposed method under the condition of bad data. Based on the scenarios above, the following scenarios are considered as follows.

Scenario VI: Randomly select some of the measurements, set them as bad data, and execute the control strategies directly without bad data identification.

In this paper, 20% of the measurement values are randomly set as bad data. The bad data is generated with the real data multiplied by the error factor from a uniform distribution with the interval [0, 0.3]. Ten simulation cases are performed. Bad data identification results are shown in Table IV, and three of the bad data identification results are shown in Fig. 16. The red circle is the true value of the bad data, while the blue triangle is the estimated value of the bad data. It can be seen that the GIST method can effectively identify the bad data in the measurements, which lays the foundation for the robust control of ADNs.

TABLE IV

BAD DATA IDENTIFICATION RESULTS

| Number of simulations | Number of bad data | Number of bad data identified | Bad data identification rate |
|---|---|---|---|
| 10 | 10 | 10 | 100% |

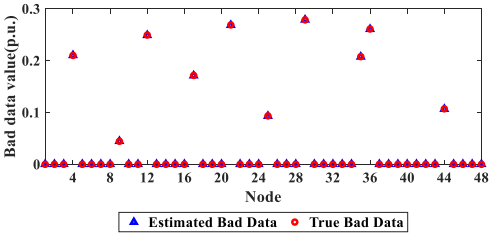


(a) Bad data identification results of case 1.

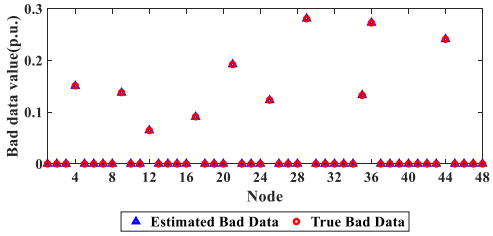


(b) Bad data identification results of case 2.

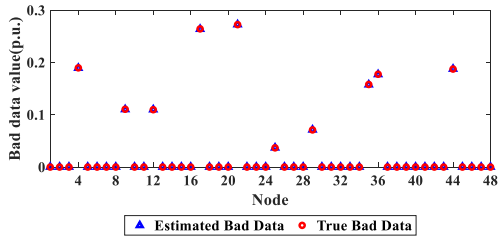


(c) Bad data identification results of case 3.

Fig. 16. Bad data identification results.

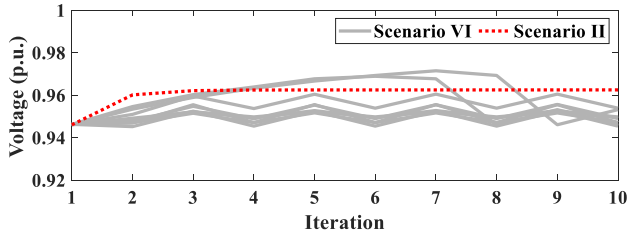


(a) Voltage iteration of node 9 at 19:00.

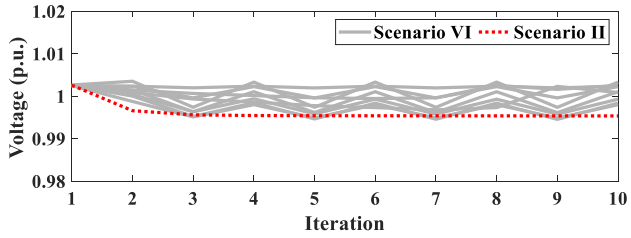


(b) Voltage iteration of node 36 at 19:00.

Fig. 17. Comparison of voltage control performances of Scenarios II and VI.

Fig.17 shows the comparison of the voltage control performances of Scenarios II and VI. It can be seen that the voltage of each node in Scenario VI can not converge to the optimal value owing to the bad data. However, the nodal voltages in Scenario II can still ensure satisfactory convergence, which effectively improves the robustness. Specifically, Fig. 17(a) and (b) show that the voltage of nodes 9 and 36 will oscillate and cannot achieve stable convergence in Scenario VI owing to the addition of bad data at these nodes. In contrast, after identifying and eliminating the bad data by the GIST method, the iterations can still converge within a few steps, which illustrates that the proposed method can effectively deal with the bad data and improve control robustness.

### *E. Scalability Analysis*

The modified IEEE 123-node distribution network is adopted to verify the scalability of the proposed data-driven method. Fig. 18 shows the topology of the test system. Six PVs with a capacity of 1000 kWp and three WTs with a capacity of 1000 kVA are integrated into the distribution network. A multi-terminal SOP is deployed among nodes 61, 117, and 123. The capacity of each converter of multi-terminal SOP is set to 3.0 MVA. The Scenarios I and II in Section IV.A are also carried out in the test case.

The control performance is demonstrated in Table V. The improvement of multi-mode adaptive control is obvious in Scenario II. Compared with Scenario I, the $VDI$, $LBI$, and power loss are diminished by 27.45%, 55.58% and 53.60% respectively. Thus, the proposed data-driven multi-mode control method can effectively satisfy the diverse operational requirements.

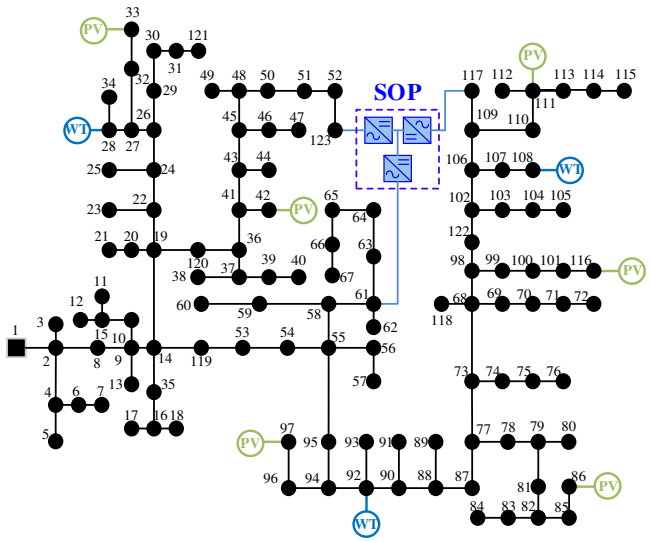


Fig. 18. Structure of IEEE 123-node distribution network.

TABLE V

CONTROL PERFORMANCES OF THE IEEE 123-NODE SYSTEM

| Scenario | Minimum voltage (p.u.) | Maximum voltage (p.u.) | $VDI$ (p.u.) | $LBI$ (p.u.) | Power loss (kW) |
|---|---|---|---|---|---|
| I | 0.9028 | 1.0660 | 0.0357 | 30.3518 | 880.8925 |
| II | 0.9228 | 1.0214 | 0.0259 | 13.4814 | 408.7404 |

The discussion of the relationship between computational burden and node number of large-scale systems is also provided, as shown in Table VI. The data-driven SOP control problem scales with the number of nodes in distribution networks, and the computational time grows approximately linearly. In practical operation, distribution networks are generally divided into several regions of similar size. The computational time can meet the requirement of the control horizon, which is set to 20 seconds in this paper. Thus, the proposed data-driven multi-mode control method can be implemented in practical applications.

TABLE VI

COMPUTATIONAL EFFICIENCY OF CONTROL PROCESS

| Test case | Average number of convergence steps | Average calculation time in each iteration (second) |
|---|---|---|
| Practical distribution network | 4 | 0.4286 |
| Modified IEEE 123-node distribution network | 7 | 1.0884 |

In summary, the proposed multi-mode data-driven control method can effectively alleviate the impact of DG integration and satisfy the diverse operational requirements in ADNs. In addition, the proposed method is also suitable for large-scale systems and improving the operational performance of ADNs.

## V. CONCLUSIONS

To meet diverse operational requirements in complex operational environments, this paper proposes a data-driven mul-

ti-mode adaptive control method for SOP with bad data. First, considering the inaccurate network parameters and quality of measurement data, a robust data-driven framework for SOP operation is proposed based on the robust HO-RLS method to determine the accurate response function. Then, multi-mode adaptive control for the SOP is designed to improve the flexibility of the system operation. The results show that the proposed method can fully explore the potential benefits of SOP to adaptively respond to different operational requirements and improve the operational performance of ADNs.

Future research can be conducted from the following perspectives. First, there are multiple flexible resources with different time scales in ADNs. Coordinating SOP with multiple flexible resources will further improve the control effectiveness. Second, the development of edge computing makes it possible for the local control to respond quickly to DG fluctuations. Local data-driven methods of SOP can be further investigated.

## REFERENCES


[1] T. Ding, Z. Wang, M. Qu, Z. Wang and M. Shahidehpour, "A sequential black-start restoration model for resilient active distribution networks," *IEEE Trans. Power Syst.*, vol. 37, no. 4, pp. 3133-3136, 2022.

[2] X. Jiang, Y. Zhou, W. Ming, P. Yang and J. Wu, "An overview of soft open points in electricity distribution networks," *IEEE Trans. Smart Grid*, vol. 13, no. 3, pp. 1899-1910, 2022.

[3] T. Zhang, Y. Mu, H. Jia, X. Wang and T. Pu, "Successive MISOCP algorithm for islanded distribution networks with soft open points," *CSEE J. Power Energy Syst.*, vol. 9, no. 1, pp. 209-220, 2023.

[4] W. Cao, J. Wu, N. Jenkins, C. Wang and T. Green, "Operating principle of soft open points for electrical distribution network operation," *Appl. Energy*, vol. 164, pp. 245-257, 2016.

[5] C. Wang, J. Sun, M. Huang, X. Zha and W. Hu, "Two-stage optimization for active distribution systems based on operating ranges of soft open points and energy storage system," *J. Mod. Power Syst. Clean Energy*, vol. 11, no. 1, pp. 66-79, 2023.

[6] F. Sun, J. Ma, M. Yu and W. Wei, "Optimized two-time scale robust dispatching method for the multi-terminal soft open point in unbalanced active distribution networks", *IEEE Trans. Sustain. Energy*, vol. 12, no. 1, pp. 587-598, 2021.

[7] J. Jian et al., "Supply restoration of data centers in flexible distribution networks with spatial-temporal regulation," *IEEE Trans. Smart Grid*, vol. 15, no. 1, pp. 340-354, Jan. 2024.

[8] S. Mudaliyar and S. Mishra, "Real-time coordinated control of low-voltage DC distribution network with soft opening point," *IEEE Trans. Power Electron.*, vol. 36, no. 6, pp. 7123-7137, 2021.

[9] X. Wang et al., "A two-layer control strategy for soft open points considering the economical operation area of transformers in active distribution networks," *IEEE Trans. Sustain. Energy*, vol. 13, no. 4, pp. 2184-2195, 2022.

[10] Z. Liu and L. Wang, "A robust strategy for leveraging soft open points to mitigate load altering attacks," *IEEE Trans. Smart Grid*, vol. 13, no. 2, pp. 1555-1569, 2022.

[11] X. Yang, C. Xu, Y. Zhang, W. Yao, J. Wen and S. Cheng, "Real-time coordinated scheduling for ADNs with soft open points and charging stations," *IEEE Trans. Power Syst.*, vol. 36, no. 6, pp. 5486-5499, 2021.

[12] J. Li, et al., "Distributed online voltage control in active distribution networks considering PV curtailment," *IEEE Trans. Ind. Informat.*, vol. 15, no. 10, pp. 5519-5530, 2019.

[13] R. Babu, S. Raj, B. Bhattacharyya, "Weak bus-constrained PMU placement for complete observability of a connected power network considering voltage stability indices," *Prot. Control Mod. Power Syst.*, vol. 5, pp. 28, 2020.

[14] H. Cui, F. Li and K. Tomsovic, "Cyber-physical system testbed for power system monitoring and wide-area control verification," *IET Energy Syst. Integr*., vol. 2, pp. 32-39, 2020.

[15] Y. Liu, Z. Li and S. Sun, "A data-driven method for online constructing linear power flow model," *IEEE Trans. Ind. Appl.*, vol. 59, no. 5, pp. 5411-5419, 2023.

[16] N. Liu, C. Li, L. Chen and J. Wang, "Hybrid data-driven and model-based distribution network reconfiguration with lossless model reduction," *IEEE Trans. Ind. Informat.*, vol. 18, no. 5, pp. 2943-2954, 2022.

[17] Ning Zhao, Fengqi You, "New York State's 100% renewable electricity transition planning under uncertainty using a data-driven multistage adaptive robust optimization approach with machine-learning," *Adv. Appl. Energy*, vol. 2, pp. 100019, 2021.

[18] D. Cao, W. Hu, J. Zhao, Q. Huang, Z. Chen and F. Blaabjerg, "A multi-agent deep reinforcement learning based voltage regulation using coordinated PV inverters," *IEEE Trans. Power Syst.*, vol. 35, no. 5, pp. 4120-4123, 2020.

[19] H. Liu and W. Wu, "Federated reinforcement learning for decentralized voltage control in distribution networks," *IEEE Trans. Smart Grid*, vol. 13, no. 5, pp. 3840-3843, 2022.

[20] X. Sun, et al., "A multi-mode data-driven volt/var control strategy with conservation voltage reduction in active distribution networks," *IEEE Trans. Sustain. Energy*, vol. 13, no. 2, pp. 1073-1085, 2022.

[21] Y. Huo et al., "Data-driven adaptive operation of soft open points in active distribution networks," *IEEE Trans. Ind. Informat.*, vol. 17, no. 12, pp. 8230-8242, 2021.

[22] J. -W. Chang, M. Kang and S. Oh, "Data-driven estimation of voltage-to-power sensitivities considering their mutual dependency in medium voltage distribution networks," *IEEE Trans. Power Syst.*, vol. 37, no. 4, pp. 3173-3176, 2022.

[23] J. Zhang, Z. Chen, C. He, Z. Jiang and L. Guan, "Data-driven-based optimization for power system var-voltage sequential control," *IEEE Trans. Ind. Informat.*, vol. 15, no. 4, pp. 2136-2145, 2019.

[24] K. Slavakis and S. Banerjee, "Robust hierarchical-optimization RLS against sparse outliers," *IEEE Trans. Signal Process. Lett.*, vol. 27, pp. 171-175, 2020.

[25] S. Li, W. Wu and Y. Lin, "Robust data-driven and fully distributed volt/var control for active distribution networks with multiple virtual power plants," *IEEE Trans. Smart Grid*, vol. 13, no. 4, pp. 2627-2638, 2022.

[26] S. Lakshminarayana, A. Kammoun, M. Debbah and H. V. Poor, "Data-driven false data injection attacks against power grids: a random matrix approach," IEEE Trans. Smart Grid, vol. 12, no. 1, pp. 635-646, 2021.

[27] H. Wang et al., "Dynamic data injection attack detection of cyber physical power systems with uncertainties," *IEEE Trans. Ind. Informat*., vol. 15, no. 10, pp. 5505-5518, 2019.

[28] E. Dall'Anese and A. Simonetto, "Optimal power flow pursuit," *IEEE Trans. Smart Grid*, vol. 9, no. 2, pp. 942-952, 2018.

[29] A. S. Zamzam, X. Fu, and N. D. Sidiropoulos, "Data-driven learning-based optimization for distribution system state estimation," *IEEE Trans. Power Syst.*, vol. 34, no. 6, pp. 4796-4805, 2019.

[30] J. Zhao, G. Zhang, M. L. Scala and Z. Wang, "Enhanced robustness of state estimator to bad data processing through multi-innovation analysis," *IEEE Trans. Ind. Informat.*, vol. 13, no. 4, pp. 1610-1619, 2017.

[31] Y. Lin and A. Abur, "A highly efficient bad data identification approach for very large scale power systems," *IEEE Trans. Power Syst.*, vol. 33, no. 6, pp. 5979-5989, 2018.

[32] P. Gong, et al., "Ageneral iterative shrinkage and thresholding algorithm for non-convex regularized optimization problems," *Proc. Int. Conf. Mach. Learn.*, 2013, pp. II–37–II–45.

[33] J. Zhao et al., "Robust operation of flexible distribution network with large-scale EV charging loads," *IEEE Trans. Transp. Electr.*, 2023 early access.

[34] Lofberg J. YALMIP: A toolbox for modeling and optimization in MATLAB. *2004 IEEE International Symposium on Computer Aided Control Systems Design*, Taipei, Taiwan, 2004. pp. 284–289.

[35] J. Zhao, et al., "Peer-to-peer electricity trading of interconnected flexible distribution networks based on non-cooperative games". *Int. J. Elec. Power*, vol. 145, pp. 108648, 2023.

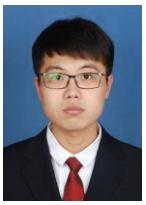

**Shiyuan Gao** (Graduate Student Member, IEEE) received the B.S. degree in electrical engineering from Tianjin University, Tianjin, China, in 2019. He is currently working toward the Ph.D. degree in electrical engineering with Tianjin University, Tianjin, China.

His current research interests include optimal operation and data-driven operation of distribution networks.

**Peng Li** (Senior Member, IEEE) received the B.S. and Ph.D. degrees in electrical engineering from Tianjin University, Tianjin, China, in 2004 and 2010, respectively.

He is currently a Professor with the School of Electrical and Information Engineering, Tianjin University. His current research interests include operation and planning of active distribution networks, modeling, and transient simulation of power systems. Prof. Li is an Associate Editor of IEEE Transactions on Sustainable Energy, CSEE Journal of Power and Energy Systems, Sustainable Energy Technologies and Assessments, and IET Renewable Power Generation.

**Haoran Ji** (Member, IEEE) received the B.S. and Ph.D. degrees in electrical engineering from Tianjin University, Tianjin, China, in 2014 and 2019, respectively.

From 2019 to 2021, he was a Postdoctoral Research with Tianjin University. He is currently an Associate Professor with Tianjin University. His research interests include distributed generation systems and optimal operation of distribution networks. He was supported by China National Postdoctoral Program for Innovative Talents in 2019.

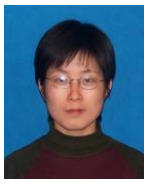

**Jinli Zhao** (Member, IEEE) received the Ph.D. degree in electrical engineering from Tianjin University, Tianjin, China, in 2007. She is currently an Associate Professor in the School of Electrical and Information Engineering, Tianjin University.

Her research interests include operation and planning of active distribution networks, and power system security and stability.

**Hao Yu** (Senior Member, IEEE) received the B.S. and Ph.D. degrees in electrical engineering from Tianjin University, Tianjin, China, in 2010 and 2015, respectively. He is currently an Associate Professor with the School of Electrical and Information Engineering, Tianjin University.

His current research interests include the operation analysis and optimization of active distribution networks and integrated energy systems. He is the assistant editor of IET Energy Systems Integration.

**Jianzhong Wu** (Fellow, IEEE) received the B.Sc., M.Sc., and Ph.D. degrees in electrical engineering from Tianjin University, China, in 1999, 2002 and 2004, respectively. From 2004 to 2006, he was at Tianjin University, where he was an Associate Professor. From 2006 to 2008, he was a Research Fellow at the University of Manchester, Manchester, U.K. He is a Professor of Multi-Vector Energy Systems and the Head of the School of Engineering, Cardiff University, U.K. His research interests include integrated multi-energy infrastructure and smart grid. He is Co-Editor-in Chief of Applied Energy. He is the Co-Director of U.K. Energy Research Centre and EPSRC Supergen Energy Networks Hub.

**Chengshan Wang** (Senior Member, IEEE) received the Ph.D. degree in electrical engineering from Tianjin University, Tianjin, China, in 1991.

He is currently a Professor with the School of Electrical and Information Engineering, Tianjin University. Prof. Wang is a Member of Chinese Academy of Engineering. His research interests include distribution system analysis and planning, distributed generation system and microgrid. Prof. Wang is the Editor-in-Chief of IET Energy Systems Integration. He is the Director of the Key Laboratory of Smart Grid of Ministry of Education, Tianjin University, Tianjin, China.